Arabian Journal for Science and Engineering
https://doi.org/10.1007/s13369-026-11373-0

RESEARCH ARTICLE-MECHANICAL ENGINEERING

Revealing the Influence of Hafnium on the Microstructure, Corrosion, and Wear Properties of Fe–10Cr Alloy

Mahmut Erol[1] · Gürkan Tarakçı[2] · Burçin Özbay Kısasöz[3] · Yahya Bayrak[3] · Alptekin Kısasöz[3]

Received: 17 January 2026 / Accepted: 23 April 2026

Abstract

The study aimed to reveal the influence of hafnium addition on the characteristics of Fe-10Cr alloy. Fe-10Cr alloys containing varying hafnium additions (0–3 wt%) were fabricated by plasma arc melting to investigate the effect of hafnium on microstructural evolution, mechanical properties, wear behavior, and corrosion performance. Microstructural characterization was conducted using SEM, EDS, EBSD, and XRD techniques. The results indicated that low hafnium additions (0.5–1 wt%) led to grain coarsening due to insufficient heterogeneous nucleation, whereas higher hafnium contents ($\geq$ 2 wt%) promoted significant grain refinement through the formation of Hf-rich intermetallic phases, including Fe_2Hf, $FeHf_2$, and Cr_2Hf. These intermetallic phases acted as effective heterogeneous nucleation sites and inhibited grain growth. The addition of hafnium resulted in reduced hardness and wear resistance, primarily attributed to the diminished solid-solution strengthening and increased microstructural heterogeneity caused by grain boundary segregation. In contrast, corrosion resistance improved markedly with increasing hafnium content, as demonstrated by a noble shift in corrosion potential, reduced corrosion current density, enhanced passivation behavior, and increased impedance response. The enhanced corrosion performance was attributed to the formation of stable and protective Hf-containing passive films, particularly in alloys containing 2 and 3 wt.% hafnium. Overall, the findings reveal a clear trade-off between hardness, wear performance, and corrosion resistance in Fe–Cr–Hf alloys, providing insights for tailoring alloy compositions for specific industrial applications.

Keywords Fe–Cr–Hf alloy · Plasma arc melting · Electrochemical corrosion · Dry sliding wear

1 Introduction

Iron-chromium alloys are widely used in high-temperature processes, aggressive corrosion environments and applications need higher mechanical strength and wear resistance, such as heat exchangers, power generation, nuclear applications, energy conversion, and marine industry [1–5]. The improved corrosion and oxidation behavior of the iron-chromium alloys arises via a passivated surface formed by a stable chromium oxide film [6]. On the other hand, combined mechanical and corrosive effects can cause a degradation for the properties of the alloy and reduction in the service life [7, 8]. Moreover, improvements in the corrosion properties of iron-chromium alloys are one of the key factors that enhance the efficiency and reliability of the alloy in its area of application [9].

Properties of the iron-chromium alloys can be improved via formation of the iron-chromium based ternary alloy by using the refractory alloying elements like zirconium, niobium, yttrium, tantalum, and hafnium [5, 10–14]. Laves phase is the common phase that emerged in the microstructure of iron-based ternary alloys. The Laves phase is an intermetallic with an A_2B-type structure. Although the formation of the Laves phase influences the overall properties of the alloy, factors such as its morphology, size, and distribution within the matrix are the key parameters determining its effect on those properties [15–19]. Hafnium is one of the primary elements that promote the formation of the Laves phase in the iron–chromium system. Kobayashi and Hibaru [20] reported that Fe_2Hf type Laves phase can precipitate in Fe-9Cr alloy via interphase precipitation or accompanying the

✉ Alptekin Kısasöz
akisasoz@yildiz.edu.tr

1 Department of Materials, University of Oxford, Parks Road, Oxford OX1 3PH , UK

2 Aluminium Test Training and Research Center (ALUTEAM), Fatih Sultan Mehmet Vakif University, Istanbul , Türkiye

3 Department of Metallurgical and Materials Engineering, Yildiz Technical University, Istanbul , Türkiye

Published online: 21 May 2026

delta ferrite–austenite transformation. Moreover, Fe–Nb–Hf and Fe–Ta–Hf systems are remarkable examples of hafnium containing Laves phases [21, 22].

The hafnium addition not only provides a pronounced effect on the microstructural characteristics but also leads to significant changes in the mechanical, physical, and oxidation properties of iron-based alloys. Auger et al. [23] produced Fe-14Cr-0.22Hf alloy with spark plasma sintering. The existence of hafnium caused the precipitation of hafnium and oxide rich phases, and the dispersion strengthening mechanism increased the hardness of the alloy. Also, Xu et al. [24] studied hafnium addition in Fe-14Cr system, and it was revealed that hafnium improved the thermal stability of the alloy. Moreover, Geanta et al. [25] observed that oxidation resistance of the Fe–Cr alloy could be developed with the combined addition of aluminum and hafnium. On the other hand, Wulin et al. [26] reported the beneficial effect of hafnium on the crack susceptibility. The Fe–Cr-based clad layer was produced with hafnium addition, and the 0.9% hafnium addition prevented the cracking of the structure. Despite these potential advantages, systematic studies on iron, chromium, and hafnium alloys remain limited, particularly regarding the relationship between processing parameters, microstructural evolution, and combined corrosion-wear performance.

Accordingly, the study aims to produce Fe–Cr–Hf alloys and evaluate their microstructure, corrosion and wear behaviors. Moreover, it has been sought to elucidate the role of hafnium in properties of the iron, chromium, and hafnium ternary alloys. For this purpose, the microstructural characteristics were determined, and the corrosion and wear behaviors were investigated using electrochemical techniques and dry sliding wear tests, respectively.

2 Materials and Method

The compositions of the five designed ferrous alloys with varying hafnium additions used in this study are presented in Table 1. High-purity raw materials (≥ 99%), including Fe, Cr, and Hf metals (Nanografi), were used for alloy fabrication. The alloys were produced using a plasma arc melting furnace under a high-purity argon atmosphere. Each 25 g button-shaped alloy with a 26-mm diameter was obtained after flipping and remelted three times to ensure chemical homogeneity. The target composition was Fe–10Cr with hafnium additions varying between 0.5 and 3 wt%. The actual chemical compositions (Table 1) were determined by averaging measurements taken from five different general regions. The as-cast alloys were used for corrosion and dry sliding wear tests. Prior to testing, all samples were ground using SiC papers down to 2500 grit, followed by final polishing with colloidal silica to obtain a surface suitable for microstructural characterization, corrosion, and wear tests. General microstructural observations, chemical composition analyses, and electron backscatter diffraction (EBSD) measurements were carried out using a scanning electron microscope (SEM) equipped with the relevant detectors and attachments. Moreover, energy-dispersive X-ray spectroscopy (EDS) spot analyses were performed to reveal the composition of the phases. Analyses were carried out by Jeol JSM IT-800 with APEX EDS and EBSD detectors. X-ray diffraction (XRD) analysis was performed using an X-ray diffractometer over a 2θ range of 40–120°, with a scan rate of 1°/min, to identify the phase constituents of the alloys. PANalytical Empyrean equipment was used for XRD analysis.

Vickers hardness tests were performed with 2.5 kg test load, according to ASTM E92—17. Moreover, dry sliding wear tests were performed using the 6-mm-diameter Al_2O_3 counterface at room temperature by a ball-on disk tribometer. The tests were carried out with 90 m sliding distance, 25 mm/s sliding velocity, and 30 N test loads. Volume loss values were measured with 3D profile analyses, and Eq. 1 was used to calculate the specific wear rate (ASTM G99—17):

$$\mathrm{WR} = {}^{V}/_{\mathrm{LP}} \tag{1}$$

P was the applied load, and L was the sliding distance. In addition, the average coefficient of friction (CoF) was determined, and 3D profile analysis were performed on worn surfaces.

Potentiodynamic polarization (PDP) and electrochemical impedance spectroscopy (EIS) tests were performed on produced alloys at room temperature. The tests were applied in 3.5% NaCl solution, and a triple electrode assembly was constituted including test sample as working electrode, platinum plate as counter electrode, and Ag/AgCl solution as reference electrode. Prior to tests, open-circuit potential (OCP) was measured for 30 min. The PDP tests were performed between 0.15 to 0.5 V against the OCP. The EIS tests were applied by 10 mA AC current at the OCP over a frequency range of 0.1 Hz to 100,000 Hz.

3 Results and Discussion

Figure 1 shows the SEM micrographs of the alloys. The microstructures of the hafnium-free FeCrHf-0 and 0.5 wt% hafnium containing FeCrHf-0.5 samples were nearly identical (Fig. 1a and b). It was observed that both samples consisted of single-phase structure. The solubility of chromium in iron is relatively high, and the existence of chromium promotes the formation of iron-chromium solid-solution structure [27]. Moreover, hafnium containing phases could not be determined in FeCrHf-0.5 sample due to addition of hafnium at lower ratio. The FeCrHf-1, FeCrHf-2,

Table 1 Composition of the produced alloys

Sample	Nominal composition (wt%)			Actual composition (wt%)		
	Fe	Cr	Hf	Fe	Cr	Hf
FeCrHf-0	90.0	10.0	–	90.3 ± 0.3	9.7 ± 0.3	–
FeCrHf-0.5	89.5	10.0	0.5	89.3 ± 0.4	9.8 ± 0.3	0.9 ± 0.1
FeCrHf-1	89.0	10.0	1.0	89.0 ± 0.2	9.9 ± 0.2	1.1 ± 0.2
FeCrHf-2	88.0	10.0	2.0	88.2 ± 0.3	9.7 ± 0.3	2.1 ± 0.2
FeCrHf-3	87.0	10.0	3.0	87.0 ± 0.3	9.7 ± 0.3	3.3 ± 0.3

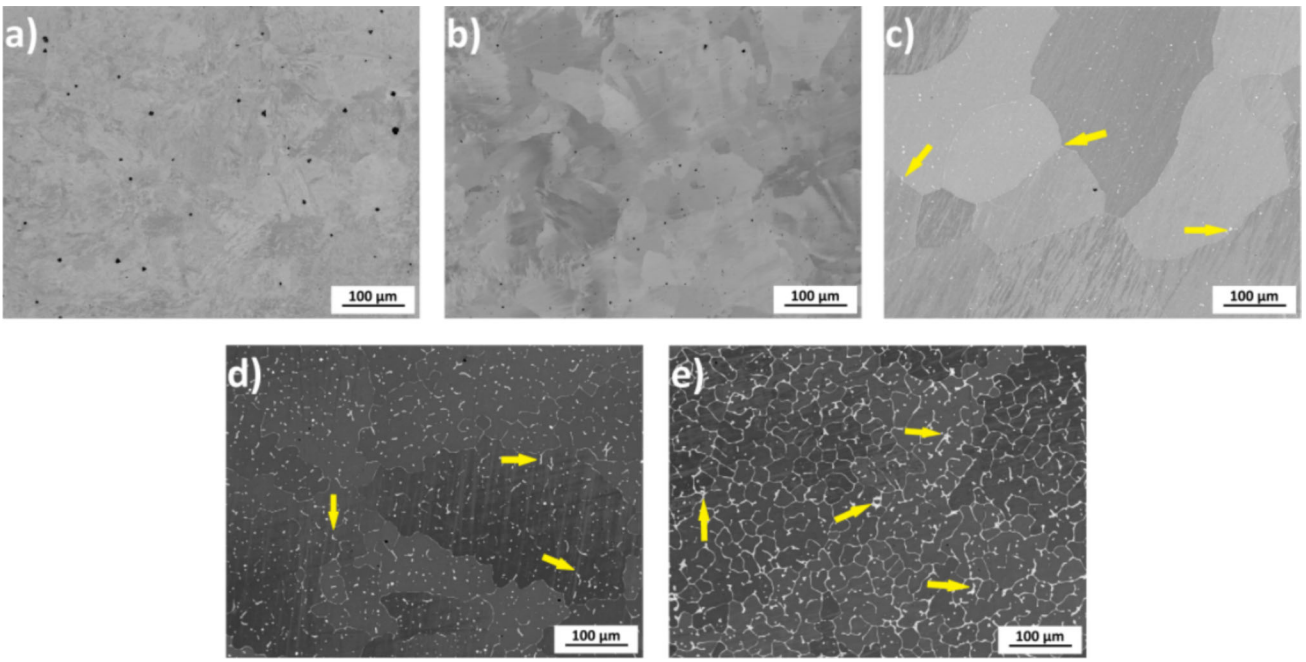

Fig. 1 SEM micrographs of the alloys produced with varied hafnium content: **a** FeCrHf-0, **b** FeCrHf-0.5, **c** FeCrHf-1, **d** FeCrHf-2, and **e** FeCrHf-3

and FeCrHf-3 samples consisted of 1 wt%, 2 wt%, and 3 wt% hafnium, respectively. For these samples, it was clearly observed that microstructural changes induced by hafnium addition, as indicated with yellow arrows (Fig. 1c-e). In particular, grain boundary segregations became markedly pronounced in the FeCrHf-2 and FeCrHf-3 with increasing hafnium content. Hafnium, as a transition metal, has low solubility in iron due to its larger atomic radius, strong chemical affinity for compound formation and crystallographic structure difference [28]. Consequently, the increase in hafnium content led to enhanced grain boundary segregation.

XRD analyses of the produced alloys are given in Fig. 2. All produced alloys included the (110), (200), (211), (220), and (310) peaks of the ferrite phase. It can be inferred that higher solubility of the chromium in iron improved the stability of ferrite phase as a matrix structure. Moreover, it was evident that ferrite peaks shifted to lower angles with increasing hafnium content. Despite the low solubility of hafnium in iron, even a small amount of dissolved hafnium caused lattice expansion in the ferritic solid-solution matrix due to its large atomic radius. Accordingly, the ferrite solid-solution diffraction peaks systematically shifted toward lower 2θ angles from FeCrHf-0 to FeCrHf-3 [29]. The XRD analysis of the FeCrHf-0 revealed that the sample only consisted of ferrite phase, compatible with SEM analysis. Similarly, 0.5 wt% and 1 wt% hafnium containing FeCrHf-0.5 and FeCrHf-1 samples exhibited XRD patterns comparable to that of the FeCrHf-0. Despite the hafnium addition, no hafnium containing phases were identified in these samples. This phenomenon can be attributed to hafnium concentrations below the detection limit of XRD, in accordance with literature [30]. The XRD analysis of the FeCrHf-2 consisted of (044), (088), (048), and (177) peaks of the $FeHf_2$, and (044) and (135) peaks of the Fe_2Hf phases, besides ferrite. On the other hand, the FeCrHf-3 sample comprised of (044), (135), and (026) peaks of the Fe_2Hf phase, (113), (133), and (335) peaks of the Cr_2Hf phase, and (012) peak of the hafnium, alongside the ferrite phase.

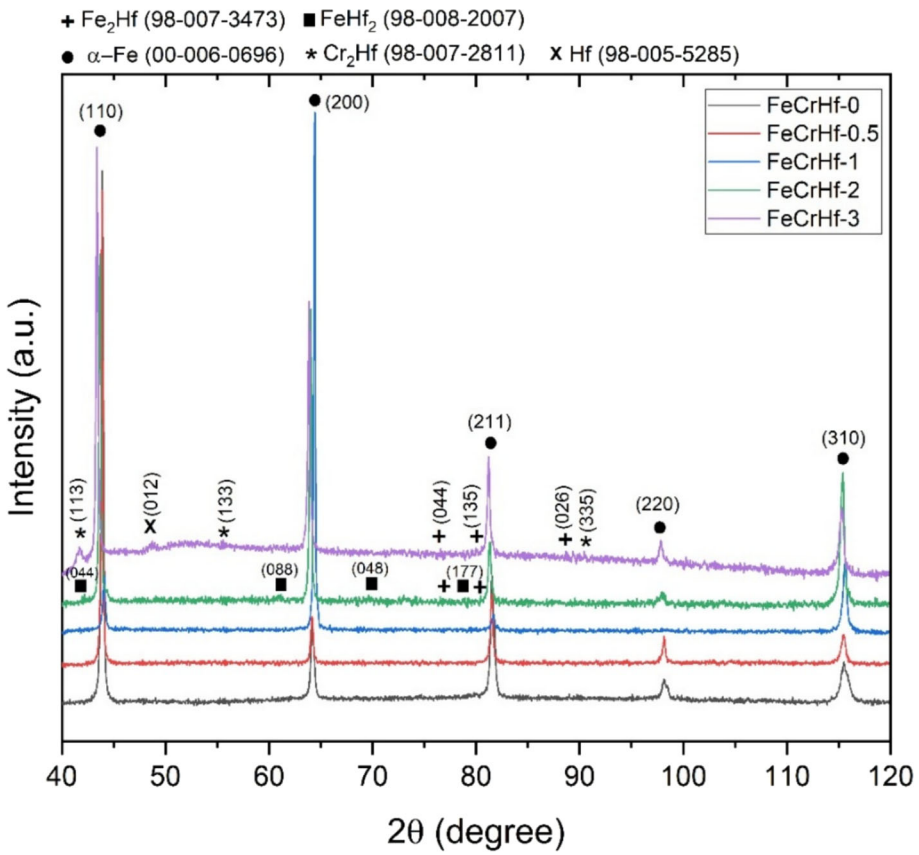

Fig. 2 XRD analysis of the alloys

The $FeHf_2$ and Fe_2Hf intermetallic phases were detected in the XRD analysis of the 2 wt% hafnium containing FeCrHf-2 sample. The formation of both intermetallics has been reported in the Fe–Hf system by various researchers [31–33]. While $FeHf_2$ is a hafnium-rich phase, the Fe_2Hf phase has a relatively lower hafnium content [34]. Especially, it was reported that hafnium-rich segregations promoted the formation of local $FeHf_2$ intermetallic [35]. As revealed by SEM analysis, significant hafnium segregation was observed along the grain boundaries. Accordingly, hafnium-rich $FeHf_2$ intermetallic composed in FeCrHf-2. However, the $FeHf_2$ tended to transform into the more stable Fe_2Hf phase [36]. In the FeCrHf-3 sample, the low-stability $FeHf_2$ phase was not detected, and it was observed that the dominant iron and hafnium-based phase was Fe_2Hf. The usage of hafnium in increasing amounts promoted the formation of the more stable Fe_2Hf phase. In addition, the presence of Cr_2Hf and metallic hafnium was also detected. It was assumed that the strong mutual affinity between iron and chromium results in extensive solid-solution formation, and it restricted the chromium and hafnium interaction in FeCrHf-2. Nevertheless, the increased hafnium content enhanced the chromium–hafnium interaction, leading to the formation of the Cr_2Hf intermetallic phase. Additionally, metallic hafnium was detected with the 3 wt% hafnium addition due to both the limited solid-solution dissolution of hafnium and the insufficient interaction of iron, chromium, and hafnium required for extensive formation of intermetallics.

EDS spots and the result of the EDS analysis can be seen in Fig. 3 and Table 2, respectively. EDS spot analyses were performed on the FeCrHf-1, FeCrHf-2, and FeCrHf-3 samples, in which the presence of hafnium was clearly observed in the general SEM analyses and different phase interactions were also identified by XRD analyses. In general, hafnium containing structures were observed to form a continuous morphology along the grain boundaries and to appear as particulates in regions near to the grain boundaries. The A1, B1, and C1 spots corresponded to the matrix structure of the samples. These regions were found to be rich in iron, containing chromium in the range of 9–10 wt%. The analysis of the matrix was consistent with the ferrite having a BCC crystal structure, as also identified in the XRD analyses. The A2, B2, and C2 spots represented analyses taken from particulate structures located near the grain boundaries. These regions were observed to consist of hafnium-rich structures containing more than 90 wt% hafnium. Nevertheless, the XRD analyses indicated that an interaction occurs between the hafnium-rich regions and the matrix structure, as observed in the SEM images. No phase formation was detected in the XRD analyses due to the

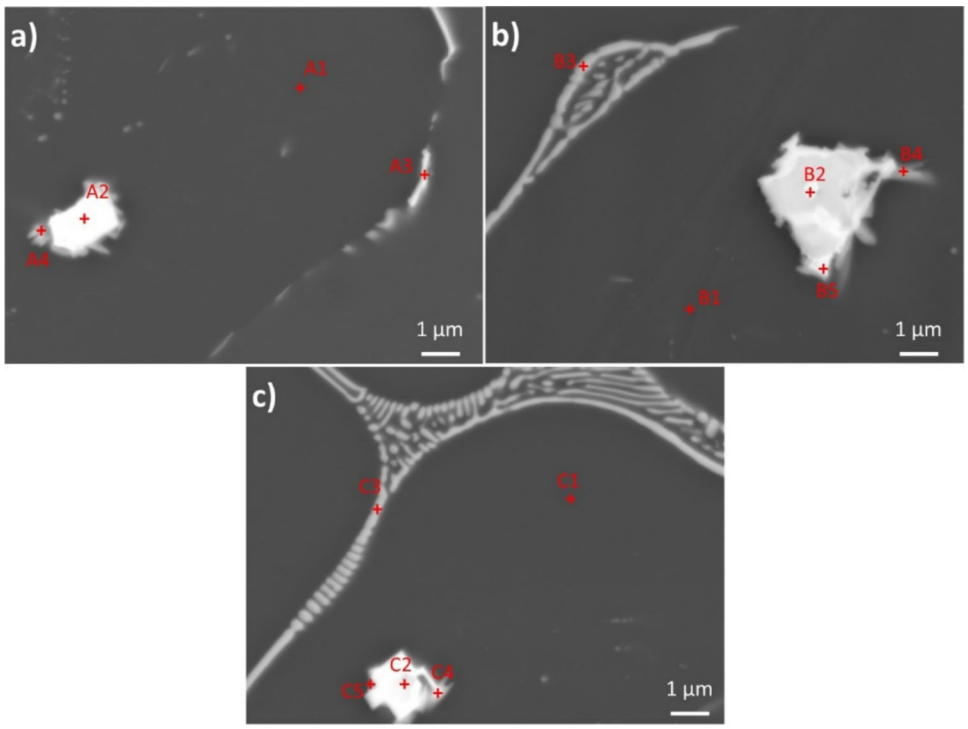

Fig. 3 SEM–EDS spots of the alloys: **a** FeCrHf-1, **b** FeCrHf-2, and **c** FeCrHf-3

Table 2 EDS spot analysis of Fig. 3 (wt%)

Samples	Spots	Fe	Cr	Hf
FeCrHf-1	A1	90.9	9.1	–
	A2	7.9	0.8	91.3
	A3	47.3	5.8	46.9
	A4	50.3	5.3	44.4
FeCrHf-2	B1	91.1	8.9	–
	B2	6.4	0.8	92.8
	B3	55.4	5.1	39.5
	B4	61.1	5.9	33.0
	B5	24.8	2.9	72.3
FeCrHf-3	C1	91.9	8.1	–
	C2	6.3	0.7	93.0
	C3	61.9	6.3	31.8
	C4	65.1	3.6	31.3
	C5	20.9	37.8	41.3

low hafnium addition, for the FeCrHf-1. However, A3 and A4 analyses revealed the presence of an interaction between iron and hafnium, indicating the formation of iron and hafnium containing phases at grain boundaries and matrix-particulate interface. For the FeCrHf-2 and FeCrHf-3 samples, EDS spot analysis results consistent with the XRD data. In the FeCrHf-2 sample, grain boundary (B3) and interfacial analyses (B4) indicating the formation of Fe_2Hf, as well as analyses (B5) corresponding to the formation of $FeHf_2$, were identified. Similar results were also obtained from the EDS analyses of the FeCrHf-3 sample. Analyses taken from the grain boundary (C3) and the interface (C4) regions indicated the presence of the Fe_2Hf. In addition, the formation of chromium-rich interfacial phases (C5) between the hafnium-rich structure and the matrix was observed. Overall, it was clearly determined that an interaction between iron and hafnium occurs even at low hafnium contents. However, iron-hafnium interface indicated the Fe_2Hf and $FeHf_2$ phases in the FeCrHf-2 and FeCrHf-3 samples. On the other hand, it was observed

that the Fe_2Hf phase was a much more dominant phase compared to $FeHf_2$ and formed distinctly at the grain boundary due to the presence of a fine-grained hafnium-rich phase.

EBSD analysis of the alloys, including inverse pole figure (IPF) maps, grain size distribution graphs, and image quality maps, can be seen in Fig. 4. The microstructure of the FeCrHf-0 sample was fragmented with many small grains and strong orientation variability, compatible with literature [37]. The grain structure was dominated by small grains with a diameter below 50 μm. On the other hand, it was clearly determined that hafnium addition caused a grain coarsening compared to FeCrHf-0. The grain structure of the FeCrHf-0.5 was dominated by a very large grain diameter, approximately at 300 μm. As mentioned earlier, hafnium had a strong tendency to segregate at grain boundaries. However, 0.5 wt% hafnium addition could not form effective, well-dispersed nuclei-forming particles. Similarly, 1 wt% hafnium still could not provide widespread effective nucleation to refine grains, in spite of introducing grain boundary heterogeneity. Grain structure became much more equiaxed and finer, with a broad distribution centered roughly at 50—150 μm for FeCrHf-2. As indicated in XRD analysis, hafnium-rich intermetallics were formed at 2 wt% hafnium, and these phases acted as heterogeneous nucleation substrates and retarded grain growth by limiting the grain boundary segregation of the Fe–Cr ferrite structure. Furthermore, the IPF and image quality maps of FeCrHf-3 revealed a more clearly observable grain refinement effect, attributed to the limited solubility of Hf and the formation of various Hf-bearing precipitates during solidification. FeCrHf-3 exhibited a finer and more refined microstructure compared to FeCrHf-0.5 and FeCrHf-1. Thus, lower hafnium additions led to grain coarsening, consistent with reduced effective nucleation density during solidification. At higher hafnium ratios, grain size was decreased due to the formation of the hafnium-based intermetallics that enhance heterogeneous nucleation and restrict grain growth. Moreover, it could be emphasized that the grain boundary phases promote the formation of misfit interfaces and associated dislocations, which induce internal stresses within the microstructure [38, 39]. Additionally, the presence of these grain boundary phases suppressed grain coarsening. Consequently, increasing the hafnium content contributed to grain refinement in the alloy system.

Figure 5 depicts the hardness and wear test results of the alloys. Hardness of the FeCrHf-0 sample was determined as 182.79 HV. It has been observed that the addition of hafnium resulted in a significant decrease in hardness values, as shown in Fig. 5a. The hardness value was measured as 115.56 HV in the FeCrHf-0.5 sample. The hardness showed a slight but gradual increase with the increase in hafnium ratio, reaching 129.44 HV in the FeCrHf-3. The iron-chromium-hafnium ternary alloys exhibited significantly lower hardness compared to the iron-chromium alloy containing 10 wt% Cr. As stated in the microstructural analyses, the grain size of the FeCrHf-0 was significantly smaller than in the iron-chromium-hafnium ternary alloys. Additionally, the formation of a solid solution was emphasized owing to chromium. Accordingly, the highest hardness values of the FeCrHf-0 could be attributed to solid-solution strengthening mechanism and Hall–Petch relationship due to the presence of finer grains [40, 41].

Specific wear rate and average CoF values can be seen in Fig. 5b. FeCrHf-0 sample exhibited a specific wear rate of 12.99×10^{-6} mm^3/Nm and a CoF of 0.58. This sample demonstrated the highest wear resistance compared to hafnium containing samples, as evidenced by the lowest specific wear rate. The fine-grained microstructure of the Fe-10Cr alloy, as revealed by EBSD analyses and microstructural investigations, was one of the most important factors contributing to the improved wear resistance. Also, the lowest CoF and highest hardness values further support the phenomenon. For the FeCrHf-0.5, the CoF value remained comparable to that of FeCrHf-0, whereas a pronounced increase in the specific wear rate was observed. Moreover, a significant deterioration in wear resistance was observed with increasing hafnium ratio. The specific wear rate and CoF values were measured as 59.17×10^{-6} mm^3/Nm and 0.76 in FeCrHf-3, respectively. The wear test results were consistent with the hardness results. The addition of hafnium led to a pronounced degradation in the wear behavior. As stated earlier, the solid-solution strengthening mechanism diminished, and microstructural heterogeneity arising from hafnium grain boundary segregation became prominent with hafnium addition. Also, a coarser-grained microstructure was observed in the hafnium containing samples compared to the Fe-10Cr alloy. These aspects led to a detrimental effect on the wear properties. In addition, oxidation of the worn surface during dry sliding wear tests has been emphasized by various researchers as a common phenomenon. The oxides formed on the worn surface can increase wear resistance and reduce surface damage by acting as a lubricating layer [42–45]. It has been reported that the addition of hafnium to iron-chromium alloys enhances oxidation resistance [46–48]. Consequently, it was assumed that oxidation of the worn surface was suppressed in hafnium containing samples during the wear test, limiting the formation of oxides that could otherwise provide a lubricating effect. That mechanism contributed to the high wear resistance and lowest CoF value observed in the FeCrHf-0.

Figure 6 shows the 3D profile analysis of worn surfaces. It was revealed that 3D analyses of the worn surface were compatible with the average CoF and specific wear rate values. The lowest surface damage was observed for the FeCrHf-0 sample, which exhibited the best wear performance. Moreover, the maximum wear track depth was measured to be approximately 60 μm. A similar wear track

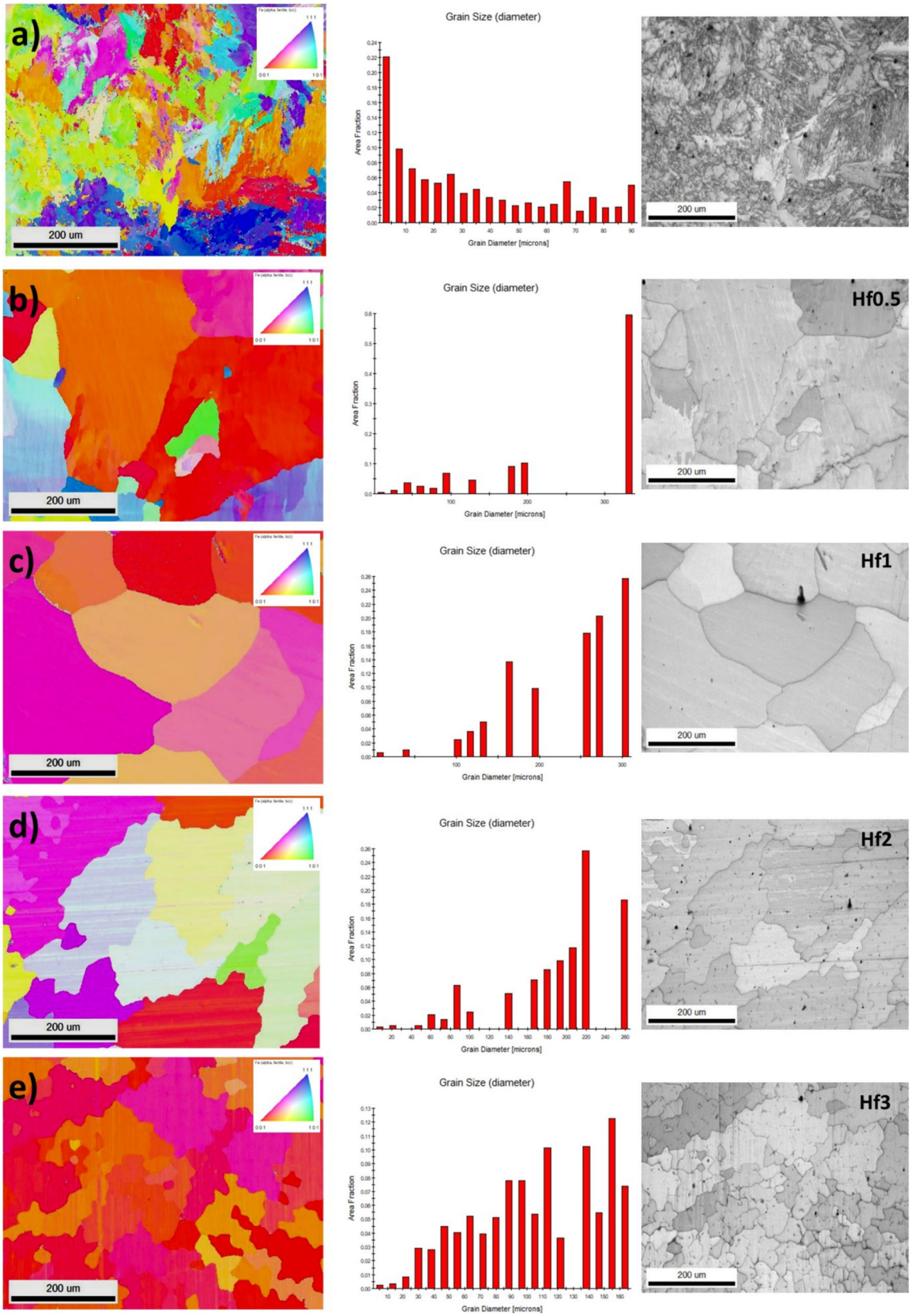

Fig. 4 EBSD analysis of the alloys: **a** FeCrHf-0, **b** FeCrHf-0.5, **c** FeCrHf-1, **d** FeCrHf-2, and **e** FeCrHf-3

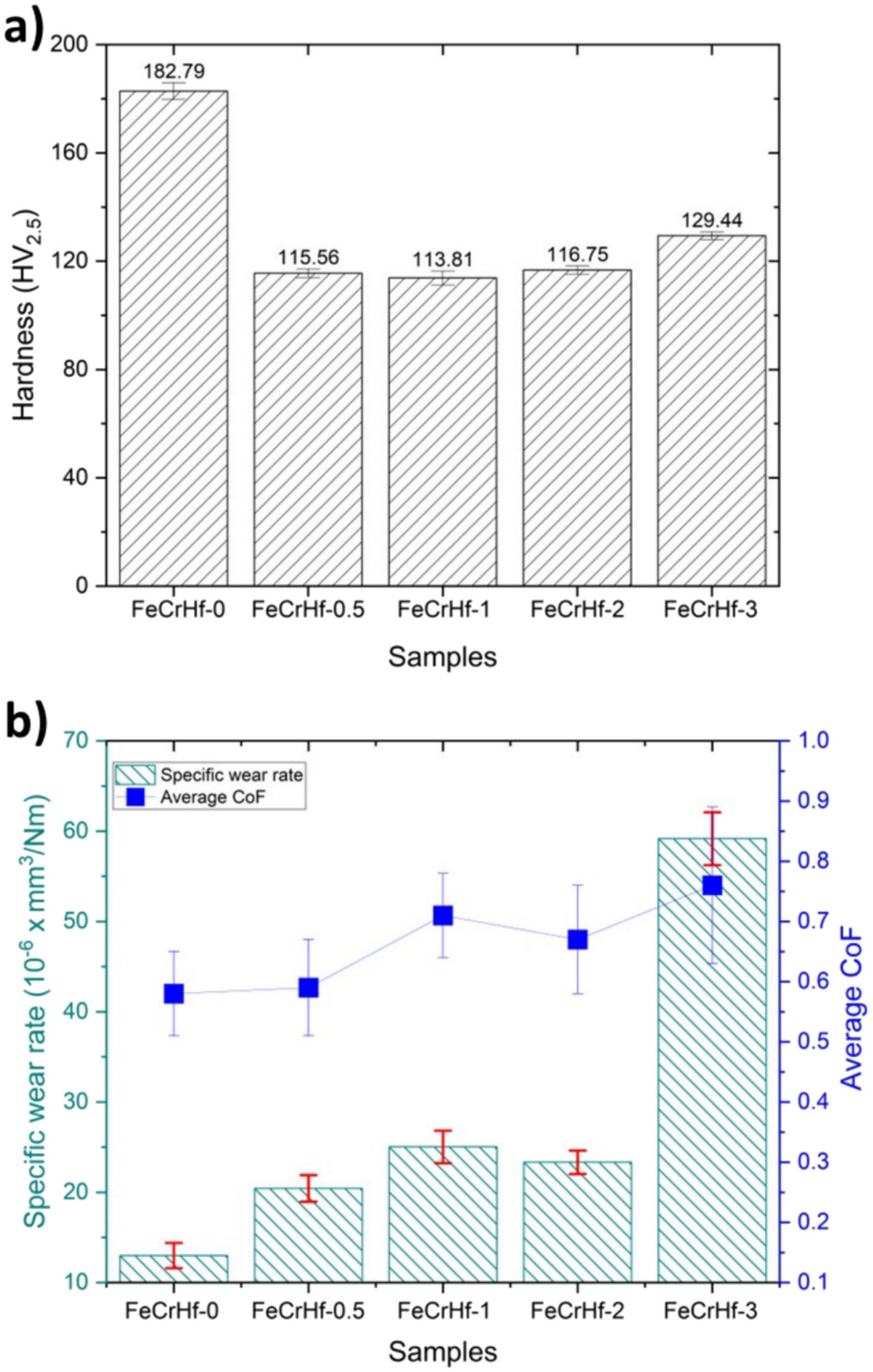

Fig. 5 **a** Hardness and **b** dry sliding wear test results

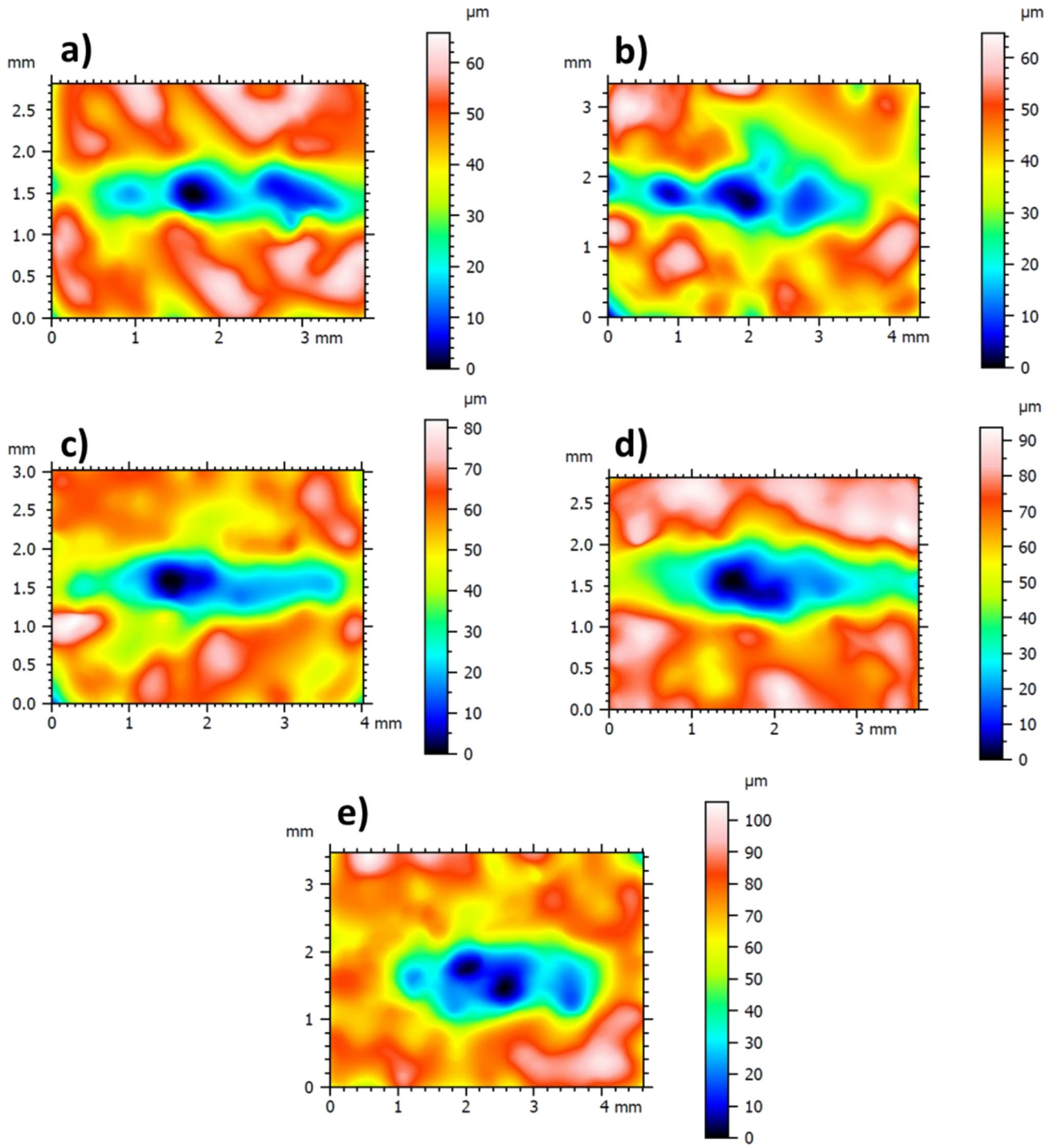

Fig. 6 3D profile analysis of the worn surfaces

profile was also obtained for FeCrHf-0.5, which showed the closest wear behavior to FeCrHf-0. As a result, the wear track depth increased with the addition of hafnium, and a wear track depth reached up to 100 μm in the FeCrHf-3 sample.

Potentiodynamic polarization curves and test results are given in Fig. 7 and Table 3, respectively. FeCrHf-0 exhibited the lowest corrosion potential and the highest current density values. This behavior indicated that FeCrHf-0 showed a higher thermodynamic tendency toward corrosion. Corrosion potential shifted toward more noble potentials with increasing hafnium ratio, suggesting that hafnium improves corrosion resistance. Moreover, the enhanced corrosion potential values of FeCrHf-2 and

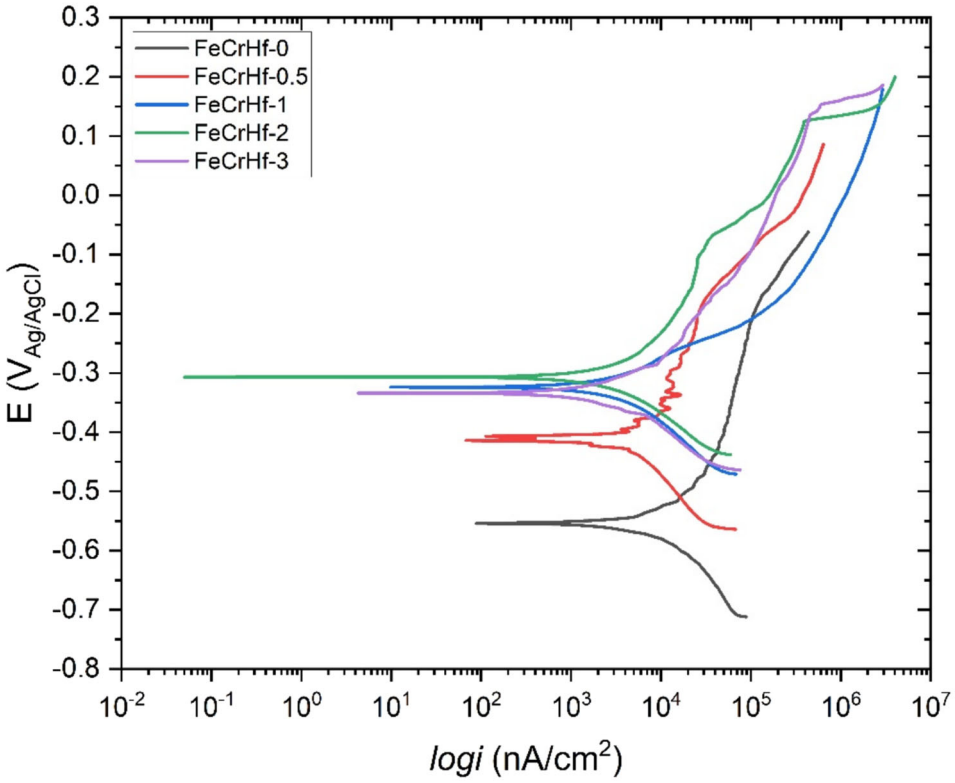

Fig. 7 Potentiodynamic polarization curves of the alloys

Table 3 Potentiodynamic polarization test results of the alloys

Sample	E_{corr} ($V_{Ag/AgCl}$)	i_{corr} (μA/cm^2)	Ba ($V_{Ag/AgCl}$/dec)	Bc ($V_{Ag/AgCl}$/dec)	Corrosion rate (mm/year)
FeCrHf-0	− 0.5480	8.967	0.160	0.171	0.1013
FeCrHf-0.5	− 0.4189	4.161	0.166	0.144	0.0470
FeCrHf-1	− 0.3268	3.047	0.083	0.110	0.0344
FeCrHf-2	− 0.3125	2.754	0.150	0.101	0.0311
FeCrHf-3	− 0.3332	1.977	0.087	0.084	0.0223

FeCrHf-3 pointed to improved surface stability of the samples [49]. On the other hand, it was clearly observed that FeCrHf-2 and FeCrHf-3 samples showed evidence of passivation. It could be attributed to the fact that hafnium promotes the formation of more protective and stable oxide layers, reducing the driving force for anodic dissolution. In addition to promoting passivation behavior in the alloy, the increase in hafnium content was also observed to raise the pitting potential when comparing 2 wt% and 3 wt% hafnium concentrations.

The highest corrosion current density (i_{corr}) implies the highest corrosion rate, while the lowest corrosion potential (E_{corr}) refers to the earliest initiation of the corrosion. The E_{corr} and i_{corr} values of the FeCrHf-0 were determined as − 0.5480 V and 8.967 μA/cm^2 in Table 3, respectively. FeCrHf-0.5 and FeCrHf-1 samples demonstrated an increase in corrosion potential, while the i_{corr} values were determined to decrease to 4.161 μA/cm^2 for FeCrHf-0.5 and 3.047 μA/cm^2 for FeCrHf-1. It could be emphasized that a systematic decrease in i_{corr} was notable even at lower hafnium ratios. Decreased i_{corr} provided slower electrochemical kinetics and improved corrosion protection [50]. Additionally, the increase in corrosion resistance became much more pronounced at higher hafnium contents. The corrosion rate, which was 0.1013 mm/year for the FeCrHf-0 sample, decreased to 0.0311 mm/year and 0.0223 mm/year for the 2 wt% and 3 wt% hafnium containing samples. Pasebani et al. [51] that oxidation of the hafnium is thermodynamically possible via internal oxidation in iron-chromium-hafnium system. Moreover, Conrath and Berthod [14] revealed the formation of HfO_2 together with Cr_2O_3 in hafnium containing iron-chromium alloys. It was stated that initial phase formed by hafnium is HfO_2 at higher hafnium concentrations. Also, HfO_2 was observed at 2

wt% and 4 wt% hafnium containing Fe-14 wt% Cr alloy [24]. The polarization results clearly demonstrate that hafnium addition significantly improved the corrosion resistance of produced alloys. The improvement was evidenced by a noble shift in corrosion potential, a marked reduction in corrosion current density, and observation of passivation. Based on the potentiodynamic polarization test results and literature, the enhanced corrosion performance of FeCrHf-2 and FeCrHf-3 alloys could be attributed to the formation of stable and protective hafnium containing passive films, which effectively suppressed active dissolution and promoted passivation.

Bode and Nyquist plots are given in Fig. 8. Bode phase angle plot indicated that produced corrosion response was dominated by one main time constant owing to single broad phase angle maximum of all samples (Fig. 8a). The highest phase angle value was obtained for the FeCrHf-3 sample. As mentioned earlier, FeCrHf-2 exhibited a pronounced passivation tendency together with FeCrHf-3, and it also showed a higher peak phase angle compared to the other samples. The finding was consistent with the lower corrosion rate values of both samples. However, the peak phase angle of FeCrHf-3 was observed to shift toward lower angle values much more rapidly than in FeCrHf-2. It has been mentioned that intermetallic phase formation occurred to a greater extent with the development of phases of different compositions. Although hafnium promotes the stability of the surface, the faster shift of the high peak phase angle toward lower values was attributed to the dissolution-enhancing effect of the intermetallic phases [52]. In addition, FeCrHf-0 shows the lowest phase angle over the whole frequency range, reflecting a less protective surface layer and faster electrochemical kinetics. On the other hand, Nyquist plots (Fig. 8b) of the samples displayed depressed semicircles related with non-ideal capacitive behavior and surface heterogeneity [53]. It can be stated that increasing semicircle diameter represents enhanced corrosion behavior [54]. FeCrHf-0 exhibited the smallest semicircle diameter referring to the lower charge transfer resistance and the poorest corrosion resistance. Progressive hafnium addition led to a systematic increase in semicircle size. It can be inferred that FeCrHf-0.5 had moderate improvement. Moreover, FeCrHf-3 provided the largest impedance response, corresponding to the largest semicircle diameter. According to Nyquist plots analysis, increasing impedance magnitude confirmed that hafnium effectively suppressed electrochemical dissolution in iron-chromium alloys.

Table 4 shows the EIS test results of the alloys. In the electrical equivalent model, the oxide film is considered to have a porous structure and to show non-ideal capacitive behavior. R1, R2, and R3 are testing solution resistance, the electrolyte resistance inside the pores, and the charge transfer resistance, respectively. Also, Q1 and Q2 are associated with the oxide film and electrical double layer [55]. The R1 values were close to each other owing to implementation of the tests in solutions with the same composition for all samples. R2 increased strongly up to 1—2 wt% hafnium addition indicating the occurrence of more resistive surface layer. The drop at 3 wt% hafnium suggested that the outer layer may not be the main contributor anymore, while the inner barrier dominates (R3). Moreover, it can be emphasized that an increase in R3 with hafnium could induce slower dissolution kinetics and improved passivation. On the other hand, Q values reflect effective capacitance of the samples. The very high Q2 values for FeCrHf-1 and FeCrHf-2 demonstrated a more heterogeneous interface compared to low hafnium containing samples. FeCrHf-3 exhibited a lower Q2 than FeCrHf-1 and FeCrHf-2 samples, together with the highest R3, which was typically interpreted as a more compact, more protective inner layer. As a result, it was stated that hafnium systematically enhanced corrosion resistance, mainly by increasing the barrier/charge transfer resistance (R3). The corrosion protection mechanism was dominated by a highly resistive inner passive layer with reduced interfacial activity.

4 Conclusion

Fe10Cr and Fe10CrHf ternary alloys with hafnium additions ranging from 0.5 to 3 wt% were successfully produced, and the effects of hafnium on microstructure, hardness, wear behavior, and corrosion performance were investigated thoroughly. The main conclusions can be summarized as follows:

-Hafnium addition significantly altered the microstructural characteristics of Fe–Cr alloys. While low hafnium contents (0.5–1 wt%) caused grain coarsening due to limited effective nucleation, higher additions (2–3 wt%) promoted grain refinement through the formation of Hf-rich intermetallic phases.

-Hardness and wear resistance decreased with 0.5—1 wt% hafnium addition, primarily due to the reduction in the efficiency of solid-solution strengthening of Fe10Cr alloy and followed by a slight increase in hardness with 2—3 wt% Hf addition.

-Corrosion resistance improved markedly with increasing hafnium content. The enhanced corrosion performance was attributed to the formation of stable and protective hafnium containing oxide layers, which suppressed active dissolution and promoted passivation.

In conclusion, hafnium addition provides a significant improvement in the corrosion resistance of Fe–Cr alloys at the expense of hardness and wear performance compared to Fe10Cr binary system. These findings offer valuable insights into the role of hafnium in Fe–Cr-based alloys and provide

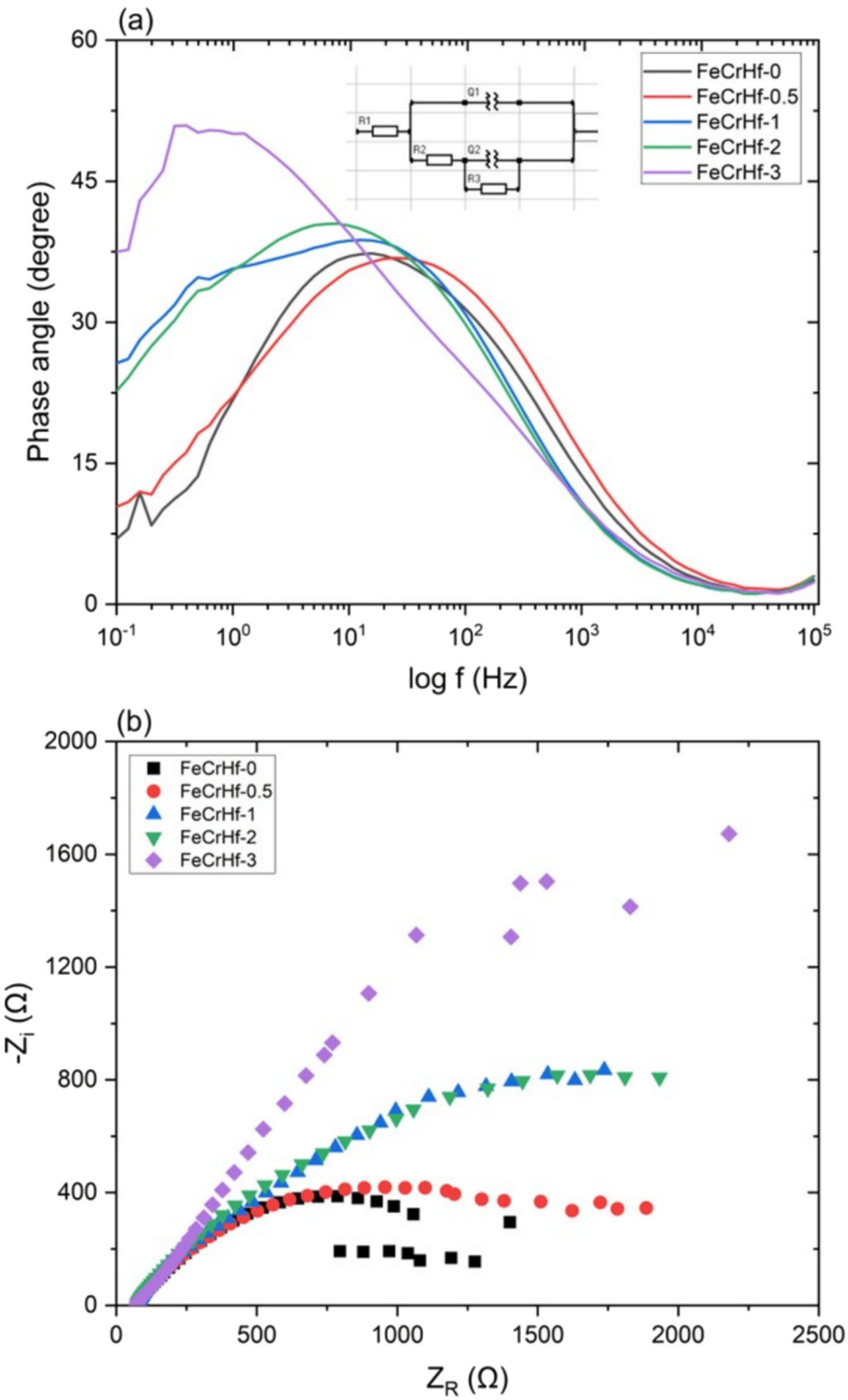

Fig. 8 **a** Phase angle Bode plots and **b** Nyquist plots of the alloys

Table 4 EIS test results of the produced alloys

Samples	R1 $R_{solution}$ (Ω)	R2 $R_{substrate}$ (R_1) (Ω)	R3 $Q_{coating}$ (Ω)	$Q_{coating}$ (Q_1) s^n/Ω	$Q_{coating}$ (Q_2) s^n/Ω
FeCrHf-0	75.92	321.1	831	$0.715 \cdot 10^{-4}$	$1.063 \cdot 10^{-4}$
FeCrHf-0.5	78.83	389.8	1311	$0.494 \cdot 10^{-4}$	$1.359 \cdot 10^{-4}$
FeCrHf-1	74.63	805.3	2229	$1.283 \cdot 10^{-4}$	$3.856 \cdot 10^{-4}$
FeCrHf-2	74.65	858.2	2087	$1.371 \cdot 10^{-4}$	$2.951 \cdot 10^{-4}$
FeCrHf-3	73.24	625.7	4450	$1.717 \cdot 10^{-4}$	$1.913 \cdot 10^{-4}$

better understanding for tailoring alloy compositions depending on the targeted balance between corrosion resistance and mechanical performance.

Funding Open access funding provided by the Scientific and Technological Research Council of Türkiye (TÜBİTAK).

Data availability The data that support the findings of this study are available within the article.

Declarations

Conflict of interest The corresponding author, on behalf of all authors, certifies that there is no conflict of interest.

References

1. Kamkumar, K.R.; Omarov, S.; Silligman, C.; Kekung, M.; Paranjape, S.; Das, P.; Roy, S.: Insights into microstructure and fretting wear behavior of additively manufactured oxide reinforced FeCrAl alloy for nuclear reactors. Tribol. Int. **219**, 111790 (2026). https://doi.org/10.1016/j.triboint.2026.111790
2. Sawada, K.; Kushima, H.; Tabuchi, M.; Kimura, K.: Microstructural degradation of Gr.91 steel during creep under low stress. Mater. Sci. Eng. A **528**(16–17), 5511–5518 (2011). https://doi.org/10.1016/j.msea.2011.03.073
3. Matijasevic, M.; Almazouzi, A.: Effect of Cr on the mechanical properties and microstructure of Fe-Cr model alloys after n-irradiation. J. Nucl. Mater. **377**(1), 147–154 (2008). https://doi.org/10.1016/j.jnucmat.2008.02.061
4. Baddoo, N.R.: Stainless steel in construction: a review of research, applications, challenges and opportunities. J. Constr. Steel Res. **64**(11), 1199–1206 (2008). https://doi.org/10.1016/j.jcsr.2008.07.011
5. Muthaiah, V.M.S.; Koch, C.C.; Mula, S.: Thermal stability and mechanical properties of Fe-Cr-Zr alloys developed by mechanical alloying followed by spark plasma sintering. J. Alloys Compd. **856**, 158266 (2021). https://doi.org/10.1016/j.jallcom.2020.158266
6. Gerard, A.Y.; Kautz, E.J.; Schreiber, D.K.; Han, J.; McDonnell, S.; Ogle, K.; Lu, P.; Saal, J.E.; Frankel, G.S.; Scully, J.R.: The role of chromium content in aqueous passivation of a non-equiatomic Ni38Fe20CrxMn21-0.5xCo21-0.5x multi-principal element alloy (x = 22, 14, 10, 6 at%) in acidic chloride solution. Acta Mater. **245**, 118607 (2023). https://doi.org/10.1016/j.actamat.2022.118607
7. Qiao, Y.; Ni, Y.; Yang, K.; Wang, P.; Wang, X.; Liu, R.; Sun, B.; Bai, C.: Iron-based high-temperature alloys: alloying strategies and new opportunities. Mater **18**, 2989 (2025). https://doi.org/10.3390/ma18132989
8. Carvalho, D.S.; Joia, C.J.B.; Mattos, O.R.: Corrosion rate of iron and iron-chromium alloys in CO_2 medium. Corros. Sci. **47**(12), 2974–2986 (2005). https://doi.org/10.1016/j.corsci.2005.05.052
9. Grice, R.J.; Faulkner, R.G.; Yin, Y.: Novel hafnium containing steels for power generation. Ironmak. Steelmak. **36**(3), 170–175 (2009). https://doi.org/10.1179/174328109X401514
10. Sheng, L.; Zhang, W.; Guo, J.; Ye, H.: Microstructure and mechanical properties of Hf and Ho doped NiAl–Cr(Mo) near eutectic alloy prepared by suction casting. Mater Charact **60**, 1311–1316 (2009). https://doi.org/10.1016/j.matchar.2009.06.00
11. Sheng, L.; Zhang, W.; Guo, J.; Zhou, L.Z.; Ye, H.Q.: Microstructure evolution and mechanical properties' improvement of NiAl–Cr(Mo)–Hf eutectic alloy during suction casting and subsequent HIP treatment. Intermet **17**, 1115–1119 (2009). https://doi.org/10.1016/j.intermet.2009.05.003
12. Zhang, X.; Wang, Q.; Kane, J.J.; Rufner, J.F.; Sun, C.: Graded microstructure and mechanical properties of spark plasma sintered Fe-Cr alloys. J. Alloys Compd. **967**, 171448 (2023). https://doi.org/10.1016/j.jallcom.2023.171448
13. Muthaiah, V.M.S.; Mula, S.: Evolution of microstructures and mechanical properties of spark plasma sintered Fe-Cr-Nb alloys. Mater. Sci. Eng. A **739**, 367–376 (2019). https://doi.org/10.1016/j.msea.2018.10.074
14. Conrath, E.; Berthod, P.: Microstructure evolution at high temperature of chromium-rich iron-based alloys containing hafnium carbides. Int. J. Mater. Res. **105**(8), 717–724 (2014). https://doi.org/10.3139/146.111085
15. Liu, B.; Sun, H.; Guo, S.; Hou, Z.; Mu, X.; Xu, L.; Zhao, D.: Structure and hydrogen storage properties of AB_2-type (A = Ti, Zr; B = Cr,Mn, Fe Co, Ni) C14 Laves phase high-entropy alloys. Intermet **188**, 109088 (2026). https://doi.org/10.1016/j.intermet.2025.109089
16. Lloyd, M.J.; Ma, K.; London, A.J.; Gibson, J.; Watson, A.: Formation of (Ti,W)Fe_2 C14 Laves phase in the W-Ti-Fe system and the impact on mechanical properties. J. Alloys Compd. **1055**, 186169 (2026). https://doi.org/10.1016/j.jallcom.2026.186169
17. Murata, Y.; Koyama, T.; Morinaga, M.; Miyazaki, T.: Prediction of the Laves Phase morphology in Fe–Cr–W–C quaternary steels with the aid of system free energy concept. ISIJ Int. **42**(12), 1423–1429 (2002). https://doi.org/10.2355/isijinternational.42.1423

18. Abe, F.: Effect of fine precipitation and subsequent coarsening of Fe_2W Laves Phase on the creep deformation behavior of tempered martensitic 9Cr-W steels. Metall. Mater. Trans. A **36**, 321–332 (2005). https://doi.org/10.1007/s11661-005-0305-y
19. Qi, X.; Li, Y.; Du, J.; Fan, W.; Bai, Y.; Chen, H.; Li, F.: Strengthening mechanism of IN 718 alloy fabricated by ultrasonic vibration-assisted laser directed energy deposition with heat treatment. J. Manuf. Process. **159**, 107–118 (2026). https://doi.org/10.1016/j.jmapro.2026.01.003
20. Kobayashi, S.; Hibaru, T.: Formation of the Fe_2Hf Laves phase along the eutectoid-type reaction path of δFe→γFe+Fe2Hf in an Fe-9Cr based alloy. ISIJ Int. **55**(1), 293–299 (2015). https://doi.org/10.2355/isijinternational.55.293
21. Shen, Q.; Zhang, Z.; de Vries, C.; Dugulan, A.I.; van Dijk, N.; Brück, E.; Li, L.: Zero thermal expansion effect and enhanced magnetocaloric effect induced by Fe vacancies in $Fe_2Hf_{0.80}Nb_{0.20}$ Laves Phase alloys. Chem. Mater. **36**(12), 6299–6305 (2024). https://doi.org/10.1021/acs.chemmater.4c01345
22. Yuan, Z.; Kobayashi, S.: Determination of phase equilibria among δ-Fe, γ-Fe and Fe_2M phases in Fe-Cr-M (M: Hf, Ta) ternary systems. Metals **12**(1), 102 (2022). https://doi.org/10.3390/met12010102
23. Auger, M.A.; Huang, Y.; Zhang, H.; Jones, C.A.; Hong, Z.; Moody, M.P.; Roberts, S.G.; Grant, P.S.: Microstructural and mechanical characterisation of Fe-14Cr-0.22Hf alloy fabricated by spark plasma sintering. J. Alloys Compd. **762**, 678–687 (2018). https://doi.org/10.1016/j.jallcom.2018.05.196
24. Xu, W.; Li, L.; Saber, M.; Koch, C.C.; Zhu, Y.; Scattergood, R.O.: Microstructures and stabilization mechanisms of nanocrystalline iron-chromium alloys with hafnium addition. Metall. Mater. Trans. A **46**(9), 4394–4404 (2015). https://doi.org/10.1007/s11661-015-2985-2
25. Geanta, V.; Voiculescu, I.; Stanciu, E.M.: Hafnium influence on the microstructure of FeCrAl alloys. IOP Conf. Ser. Mater. Sci. Eng. **133**, 012016 (2016). https://doi.org/10.1088/1757-899X/133/1/012016
26. Wulin, S.; Echigoya, J.; Beidi, Z.; Changsheng, X.; Wei, H.; Kun, C.: Vacuum laser cladding and effect of Hf on the cracking susceptibility and the microstructure of FeCrNi laser-clad layer. Surf. Coat. Technol. **126**, 76–80 (2000). https://doi.org/10.1016/S0257-8972(00)00532-6
27. Zhao, Y.; Li, Y.; Bhattacharya, A.; Poplawsky, J.D.; Henry, J.; Zinkle, S.J.: Determining the low temperature Cr solubility limit and precipitation mechanisms in Fe-Cr alloys with proton irradiations and thermal aging. Mater. Des. **256**, 114280 (2025). https://doi.org/10.1016/j.matdes.2025.114280
28. Lu, H.; Zhou, C.; Song, Y.; Zhang, Y.; Wu, Y.; Long, F.; Yao, Y.; Hao, J.; Chen, Y.; Yu, D.; Schwiedrzik, J.J.; An, K.; He, L.; Lu, z; Chen, J.: A strategy to reduce thermal expansion and achieve higher mechanical properties in iron alloys. Nat. Commun. **16**(1), 211 (2025). https://doi.org/10.1038/s41467-024-55551-w
29. Cheng, C.; Chen, C.; Chu, S.; Hu, H.; Yan, T.; Xia, X.; Feng, X.; Guo, J.; sun, D.; Wu, J.; Guo, S.; Zhang, L.: Enhancing the reversibility of lattice oxygen redox through modulated transition metal–oxygen covalency for layered battery electrodes. Adv. Mater. **34**, 2201152 (2022). https://doi.org/10.1002/adma.202201152
30. Cingöz, U.C.; Özbay Kısasöz, B.; Bayrak, Y.; Kısasöz, A.: Synergetic effect of Y_2O_3 rare-earth oxide and in-situ phases on corrosion and wear properties of AlSi10Mg aluminium matrix composites produced by hot pressing. Ceram. Int. **51**, 43111–43124 (2025). https://doi.org/10.1016/j.ceramint.2025.07.053
31. Sun, J.; Ming, C.; Yang, B.; Guo, C.; Li, C.; Du, Z.: Experimental investigation and thermodynamic description of the Fe-Hf-Nb system. J. Alloys Compd. **939**, 168696 (2023). https://doi.org/10.1016/j.jallcom.2022.168696
32. Zou, N.; Lu, H.J.; Liu, L.L.; He, Y.L.; Lu, X.G.: Experimental investigation of phase equilibria in the Fe-Hf-Zr system at 1173 K and 1373 K. Calphad **72**, 102240 (2021). https://doi.org/10.1016/j.calphad.2020.102240
33. Zhang, Z.S.; Ding, M.; Pan, F.: Magnetic properties and microstructure of vapour-deposited Fe/Hf films upon thermal annealing. J. Phys. D Appl. Phys. **33**, 185 (2000). https://doi.org/10.1088/0022-3727/33/3/303
34. H. Okamoto, Ed., *Phase Diagrams for Binary Alloys*, Second. ASM International, 2010.
35. Peng, X.; Guo, H.; Zhang, X.; Yang, W.; Luo, Y.; Li, G.: High-temperature thermal behaviour of $FeHf_2$ Laves phase heterostructures and carbon modification treatment. Mater. Sci. Eng. A **955**, 149778 (2026). https://doi.org/10.1016/j.msea.2026.149778
36. Idbenali, M.; Selhaoui, N.; Bouirden, L.; Servant, C.: Thermodynamic assessment of the Fe-Hf binary system. J. Alloys Compd. **456**, 151–158 (2008). https://doi.org/10.1016/j.jallcom.2007.02.036
37. Lu, Y.; Ying, H.; He, Y.; Hou, Y.; Li, X.; Li, F.; Zhang, H.; Zhang, L.; Wang, H.; Su, H.: Microstructure and property evolution in Fe-Cr-Ni alloys with varying Cr content fabricated by laser powder bed fusion. Mater. Today Commun. **46**, 112494 (2025). https://doi.org/10.1016/j.mtcomm.2025.112494
38. Zhao, C.C.; Ouyang, W.T.; Wen, M.; Yang, C.; Xu, D.K.; Zheng, Y.F.; Xi, T.F.; Sheng, L.Y.: Optimizing corrosion resistance of the Mg–4Zn-0.5Y-0.5Nd alloy by regulation of secondary phase and grain structure. J. Mater. Res. Technol. **35**, 435–450 (2025). https://doi.org/10.1016/j.jmrt.2025.01.062
39. Du, B.; Hu, Z.; Wang, J.; Sheng, L.; Zhao, H.; Zheng, Y.; Xi, T.: Effect of extrusion process on the mechanical and in vitro degradation performance of a biomedical Mg-Zn-Y-Nd alloy. Bioact. Mater. **5**, 219–227 (2020). https://doi.org/10.1016/j.bioactmat.2020.02.002
40. Zhang, H.; Johansson, B.; Ahuja, R.; Vitos, L.: First-principles study of solid-solution hardening in steel alloys. Comput. Mater. Sci. **55**, 269–272 (2012). https://doi.org/10.1016/j.commatsci.2011.12.020
41. Yang, G.; Kang, J.; Carsbring, A.; Mu, W.; Hedström, P.; Kim, J.K.; Park, J.H.: Heterogeneous grain size and enhanced hardness by precipitation of the BCC particles in medium entropy Fe–Ni–Cr alloys. J of Alloys Compd **931**, 167580 (2023). https://doi.org/10.1016/j.jallcom.2022.167580
42. Erol, M.; Kısasöz, A.; Yaman, P.; Karabeyoğlu, S.S.; Barut, U.: A study on high temperature dry sliding wear of AA7050-T4 and effects of the test temperature on microstructure, corrosion behavior, hardness and electrical conductivity. Mater. Today Commun. **31**, 103410 (2022). https://doi.org/10.1016/j.mtcomm.2022.103410
43. Khan, H.M.; Yilmaz, M.S.; Karabeyoğlu, S.S.; Kisasoz, A.; Özer, G.: Dry sliding wear behavior of 316 L stainless steel produced by laser powder bed fusion: A comparative study on test temperature. Mater. Today Commun. **34**, 105155 (2023). https://doi.org/10.1016/j.mtcomm.2022.105155
44. Işık, R.G.; Özbay Kısasöz, B.; Tarakçı, G.; Karabeyoğlu, S.S.; Uğuz, T.; Kısasöz, A.: Influence of high-velocity oxy-fuel sprayed Cr_3C_2-NiCr coating on corrosion and wear properties of AISI 2205. J. Mater. Eng. Perform. **34**, 2882–2896 (2024). https://doi.org/10.1007/s11665-024-09324-7
45. Tong, Y.; Zhang, T.; Zhang, S.: Influence of oxides on the formation of self-lubricating layer and anti-wear performance during sliding. Tribol. Int. **179**, 108188 (2023). https://doi.org/10.1016/j.triboint.2022.108188
46. Ishii, K.; Taniguchi, S.: Effect of La and Hf additions on the high-temperature oxidation resistance of high-purity Fe-20Cr-5Al alloy foils. Oxid. Met. **54**, 491–508 (2000). https://doi.org/10.1023/A:1004694719134

47. Dou, P.; Kimura, A.; Kasada, R.; Okuda, T.; Inoue, M.; Ukai, S.; Ohnuki, S.; Fujisawa, T.; Abe, F.; Jiang, S.; Yang, Z.: TEM and HRTEM study of oxide particles in an Al-alloyed high-Cr oxide dispersion strengthened ferritic steel with Hf addition. J. Nucl. Mater. **485**, 189–201 (2017). https://doi.org/10.1016/j.jnucmat.2016.12.001
48. Liu, X.; Chen, Y.; Lu, J.; Huang, A.; Zhang, H.; Fan, X.; Zhang, X.; Zhao, X.: A comparative study on the oxidation behavior of Y-, Hf- and YHf-doped NiCoCrAl alloys: effect of reactive elements. Corros. Sci. **218**, 111160 (2023). https://doi.org/10.1016/j.corsci.2023.111160
49. Jha, M.K.; Misra, A.; Sharma, V.S.; Alba-Baena, N.: Calcium-Driven Microstructural Evolution and Its Synergistic Effects on the Mechanical Strength, Tribological Performance, and Degradation Behavior of Mg-xCa Alloys. J. Mater. Eng. Perform. (2025). https://doi.org/10.1007/s11665-025-12938-0
50. Kisasoz, A.: Influence of solution treatment on microstructure, corrosion resistance, and oxidation behavior of cast G-NiCr28W alloy. China Foundry **16**, 63–70 (2019). https://doi.org/10.1007/s41230-019-8161-3
51. Pasebani, S.; Samimi, P.; Saber, M.: Effects of scandium and hafnium solute additions on microstructure thermal stability in nanostructured ferritic alloys. Mater Charact **151**, 216–220 (2019). https://doi.org/10.1016/j.matchar.2019.02.037
52. Pan, Z.; Luo, H.; Zhao, Q.; Cheng, H.; Li, X.: Effect of Hf addition on microstructural evolution and corrosion behavior of nickel-based alloys in hydrochloric acid. Corros. Sci. **224**, 111507 (2023). https://doi.org/10.1016/j.corsci.2023.111507
53. Mahato, N.; Singh, M.M.: Investigation of passive film properties and pitting resistance of AISI 316 in aqueous ethanoic acid containing chloride ions using electrochemical impedance spectroscopy(EIS). Port. Electrochim. Acta **29**, 233–251 (2011). https://doi.org/10.4152/pea.201104233
54. Tarakçı, G.; Özbay Kısasöz, B.; Özer, G.; Kısasöz, A.: Corrosion and wear properties of building direction dependent as-built AlSi10Mg aluminium alloy printed by selective laser melting. Mater. Chem. Phys. **342**, 130978 (2025). https://doi.org/10.1016/j.matchemphys.2025.130978
55. Mohammadi, F.; Nickchi, T.; Attar, M.M.; Alfantazi, A.: EIS study of potentiostatically formed passive film on 304 stainless steel. Electrochim. Acta **56**, 8727–8733 (2011). https://doi.org/10.1016/j.electacta.2011.07.072